How to cite: *Angew. Chem. Int. Ed.* **2022**, *61*, e202206816
International Edition: doi.org/10.1002/anie.202206816
German Edition: doi.org/10.1002/ange.202206816

Inorganic Photoelectric Crystals

Improved Polarization in the $Sr_6Cd_2Sb_6O_7Se_{10}$ Oxyselenide through Design of Lateral Sublattices for Efficient Photoelectric Conversion

Ruiqi Wang[+], Fakun Wang[+], Xian Zhang[+], Xin Feng, Chendong Zhao, Kejun Bu, Zhuang Zhang, Tianyou Zhai, and Fuqiang Huang**

Abstract: Highly-polarizable materials are favorable for photoelectric conversion due to their efficient charge separation, while precise design of them is still a big challenge. Herein a novel polar oxyselenide, $Sr_6Cd_2Sb_6O_7Se_{10}$, is rationally designed. It contains lateral sublattices of polarizable $[Sb_2OSe_4]^{4-}$ chains and highly-orientated $[CdSe_3]^{4-}$ chains. The intense polarization was evaluated by significant second-harmonic generation (SHG) signal (maximum: $12.6\times AgGaS_2$) in broad spectrum range. The polarization was found to mainly improve the carrier separation with a much longer recombination lifetime (76.5 μs) than that of the nonpolar compound $Sr_2Sb_2O_2Se_3$ (18.0 μs), resulting in better photoelectric performance. The single-crystal photoelectric device exhibited excellent response covering broad spectrum in 500–1000 nm with stable reproducibility. This work provides some new insights into the structure design of highly-polarizable heteroanionic materials for photoelectric conversion.

[*] Dr. R. Wang,[+] Prof. F. Huang
Beijing National Laboratory for Molecular Sciences, State Key Laboratory of Rare Earth Materials Chemistry and Applications, College of Chemistry and Molecular Engineering, Peking University
Beijing 100871 (P. R. China)
E-mail: huangfq@pku.edu.cn

Dr. F. Wang,[+] X. Feng, Prof. T. Zhai
State Key Laboratory of Materials Processing and Die & Mould Technology, School of Materials Science and Engineering, Huazhong University of Science and Technology (HUST)
Wuhan 430074 (P. R. China)
E-mail: zhaity@hust.edu.cn

Dr. X. Zhang[+]
Qian Xuesen Laboratory of Space Technology, China Academy of Space Technology
Beijing 100094 (P. R. China)

C. Zhao, Z. Zhang, Prof. F. Huang
State Key Laboratory of High-Performance Ceramics and Superfine Microstructure, Shanghai Institute of Ceramics, Chinese Academy of Sciences
Shanghai 200050 (P. R. China)

Dr. K. Bu
Center for High Pressure Science and Technology Advanced Research (HPSTAR)
Shanghai 201203 (P. R. China)

[+] These authors contributed equally to this work.

Introduction

The discovery of new photoelectric conversion materials has been thriving for decades due to the increasing demands for solar energy utilization. The criteria for a high-performance photoelectric conversion material include efficient generation, separation and transfer of the photo-induced charges. Among these processes, charge separation is the most challenging part to be regulated. Various strategies have been developed to promote the charge separation ability, such as heterojunction fabrication to facilitate the surface/boundary charge separation,[1] and polarization field engineering of the crystal structure (e.g. ferroelectric materials) to promote the bulk charge separation.[2] Combining the above two strategies into a single material system can theoretically achieve an overall high charge separation efficiency. Accordingly, some heterostructures containing polarizable components (e.g. $BaTiO_3/TiO_2$,[3] $BaTiO_3/MoS_2$[4]) have been developed as efficient photocatalysts, photoelectrodes or photodetectors.

In the multicomponent compounds, it is likely to form several types of sublattices containing different metal-centered polyhedra, which can be regarded as hetero-like structures at the unit-cell level. The so-called "similarity-induced aggregation" phenomenon has been explained by the widely-accepted hard and soft acids and bases (HSAB) theory. This phenomenon is quite common in the heteroanionic oxychalcogenides due to the distinct bonding abilities of O^{2-} and chalcogenide anions Q^{2-} towards metal ions.[5] The manifold structure diversity of oxychalcogenides provides an excellent platform for designing new functional materials.[6] In addition, the oxychalcogenide motifs exhibit lower symmetry, consequently generating larger local distortion and polarization.[7] These characteristics have been proved beneficial for polarization-related properties like second harmonic generation (SHG) response.[8] However, the design strategy to accommodate polar sublattices into oxychalcogenides for high charge separation efficiency has not been well developed yet.

In aim to explore new materials for efficient charge separation, we propose an ab initio structural design of polar lateral sublattices. As illustrated in Figure 1, each layer of the designed structure contains two types of sublattices, the strongly polarizable sublattice I and the highly-orientated sublattice II to accumulate the polarization. Moreover, the two sublattices are designed to form a quantum well-like electronic structure, where electrons and holes are confined in sublattice I for efficient separation.

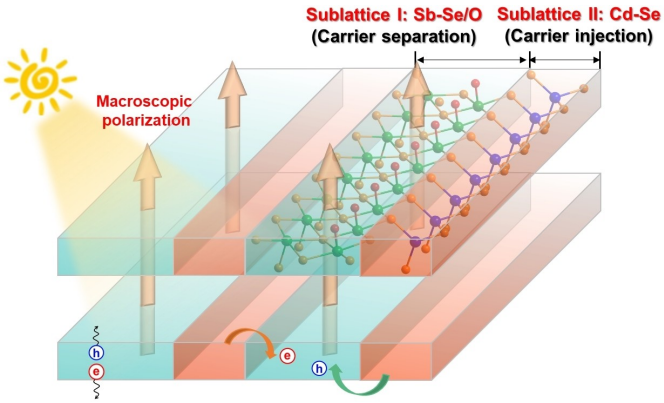

Figure 1. The scheme of lateral polar sublattices designed for efficient charge separation.

Once reassessing the polar oxysulfide $Sr_6Cd_2Sb_6O_7S_{10}$ we reported earlier,[8f] we found that it conformed well to the ideal structural type in the above scheme. The polarizable Sb–S/O sublattice was proved to endow the oxysulfide with intense SHG response. The high asymmetry and strong polarization of this sublattice can also facilitate the charge carrier separation for potential photoelectric application. However, the red oxysulfide $Sr_6Cd_2Sb_6O_7S_{10}$ possesses a relatively large band gap (1.89 eV), which impedes the full utilization and conversion of visible light. Owing to the higher energy level of Se 4*p* orbital, substituting S with Se can effectively reduce the band gap and promote visible light adsorption and conversion. Besides, strong orbital hybridization of Sb–Se in sublattice I can induce narrower energy gap than that of Cd–Se in sublattice II,[9] which can form the desired quantum well-like band alignment in the oxyselenide.

By applying the above design, a new oxyselenide, $Sr_6Cd_2Sb_6O_7Se_{10}$, featuring lateral polar sublattices of $[(Sb_2OSe_3)(CdSe_2)]^{4-}$ has been successfully synthesized. The strong polarization was reflected by the intense SHG response (maximum: $12.6\times AgGaS_2$) in broad-spectrum range. Owing to the intense polarization, $Sr_6Cd_2Sb_6O_7Se_{10}$ shows a longer carrier recombination lifetime (76.5 μs) than that of the close-related nonpolar compound $Sr_2Sb_2O_2Se_3$ (18.0 μs), indicating efficient carrier separation. Strong photoluminescence emissions at room and low temperature reflected the high crystal quality with only shallow defect states near the band edges. The single-crystal device exhibited excellent photoelectric response covering broad solar spectrum and with good reproducibility.

Results and Discussion

The crystal structure of $Sr_6Cd_2Sb_6O_7Se_{10}$ was determined by single-crystal X-ray diffraction and structural refinements. It crystallizes in the polar space group *Cm*.[10] The crystallographic data, structure refinement results and selected bond lengths and angles are shown in Table S1 and S2. This compound features a layered structure similar to its sulfide analog $Sr_6Cd_2Sb_6O_7S_{10}$.[8f] The single layer $[(Sb_2OSe_3)(CdSe_2)]^{4-}$ is constructed by two types of sublattices extending along *b* axis, as shown in Figure 2a. The sublattice I $[Sb_2OSe_4]^{4-}$ chains contain edge-sharing $[SbSe_5]^{7-}$ and $[SbOSe_4]^{7-}$ tetragonal pyramids. The sublattice II $[CdSe_3]^{4-}$ chains consist of corner-sharing $[CdSe_4]^{6-}$ tetrahedra arranged in high orientation. The two sublattices are connected via sharing the top Se atoms. $[SbO_{2.5}]^{2-}$ pseudo-chains and Sr^{2+} ions are intercalated between the anionic layers for charge balance. The detailed coordination environments are shown in Figure S1.

The highly asymmetric $[SbOSe_4]^{7-}$ and $[SbSe_5]^{7-}$ groups induce the generation of polarization electric field in sublattice I. Their dipole moments were calculated using the bond-valence approach.[11] Both groups possess large dipole moments of 15.0 Debye ($[SbOSe_4]^{7-}$) and 11.9 Debye ($[SbSe_5]^{7-}$) (Figure S2). It is worth noting that incorporating O into the chalcogenide unit can effectively increase its dipole moment, which could be positive in achieving excellent photoelectric performance. The dipole moment of sublattice I is 3.5 Debye per $[Sb_2OSe_4]^{4-}$ unit, and direction of the dipole is represented by the red arrow in Figure 2a. With the assistance of highly oriented sublattice II, the dipole of sublattice I can be accumulated to macroscopic polarization (7.0 Debye per unit cell) acting as a strong driving force for charge separation.

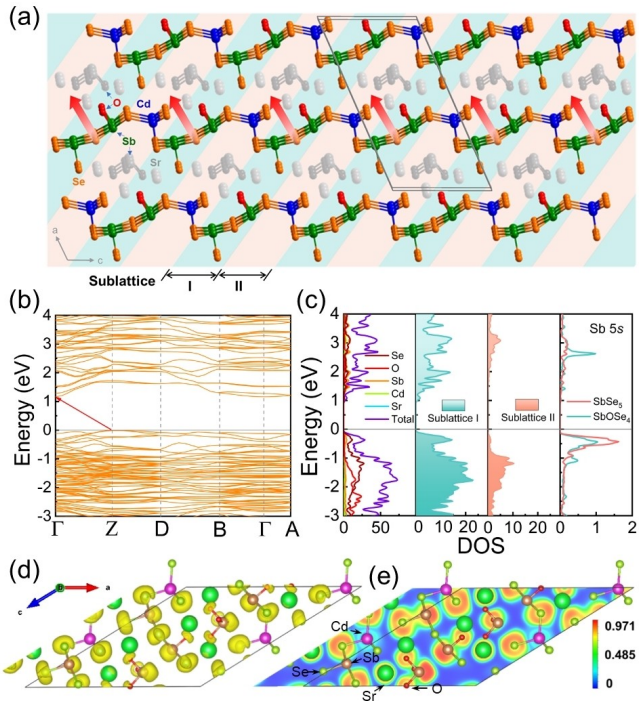

Figure 2. a) Schematic diagram of the crystal structure of $Sr_6Cd_2Sb_6O_7Se_{10}$. The red arrows represent the direction of local dipole moments of sublattice I. b) Band structure of $Sr_6Cd_2Sb_6O_7Se_{10}$. c) Total and partial DOS of elements, projected DOS of the sublattice I (green) and II (orange), projected DOS of Sb 5s in $[SbSe_5]^{7-}$ and $[SbOSe_5]^{7-}$. d) The ELF graph of $Sr_6Cd_2Sb_6O_7Se_{10}$ with an isosurface value of 0.825. e) Valence electron density map projected on the (010) plane located at $y=0.375$.

The electronic structure of the material was calculated using density functional theory (DFT) calculations. This compound is an indirect-band-gap semiconductor with the valence band maximum (VBM) located at Z point of the Brillouin zone and the conduction band minimum (CBM) at Γ point (Figure 2b). The total and partial density of states (DOS) are shown in Figure 2c and S3. The densities of states projected to the two sublattices revealed that the band edges are mainly contributed by the orbitals in sublattice I ($[Sb_2OSe_4]^{4-}$), while the main distribution of states in sublattice II ($[CdSe_3]^{4-}$) are located 1 eV away from the band edges. The narrower energy gap of sublattice I is mainly induced by strong Sb–Se orbital hybridization as well as the participation of Sb 5*s* state near the VBM (Figure S4). The projected DOS of the two sublattices reveals the formation of quantum well-like electronic structure,[12] where the photo-induced charge carrier will be confined in the highly polarizable sublattice I for efficient separation. Other details of the electronic structure were discussed in the Supporting Information.

As O possesses stronger electronegativity ($\chi_p = 3.44$) than Se ($\chi_p = 2.55$), the incorporation of O^{2-} makes appreciable effect on the electronic structure of the selenide coordination polyhedron. The DOS of Sb 5*s* states in Figure 2c and the electron localization function (ELF) graph in Figure 2d confirmed the strong lone-pair character of Sb 5*s* electrons in $[SbSe_5]^{7-}$ and $[SbOSe_4]^{7-}$ units. The electron cloud of Sb 5*s* in $[SbOSe_4]^{7-}$ is more dispersive than that in $[SbSe_5]^{7-}$, which can be distinguished clearly in the valence electron density map projected on the (010) plane at $y = 0.375$ (Figure 2e). This distinction was also clarified by comparing their partial DOS near the band edges (Figure 2c). The Sb 5*s* states in $[SbSe_5]^{7-}$ near VBM are mainly localized around −0.5 eV with a narrow distribution, while the distribution range of that in $[SbOSe_4]^{7-}$ is broader. Moreover, the Sb 5*s* states in $[SbOSe_4]^{7-}$ showed a high density around 2.5 eV in the conduction band, indicating that the 5*s* orbitals are involved in the bond forming which causes larger delocalization of Sb 5*s* electrons in $[SbOSe_4]^{7-}$. The more delocalized 5*s* electrons are easier to be polarized which should be beneficial to the charge separation.[13] These results demonstrated that the highly electronegative O can induce higher hybridization of orbitals and more dispersive 5*s* states. This mixed-anion strategy should also be effective in tuning the lone-pairs-related properties such as nonlinear optical (NLO) response and thermal conductivity.[14]

It has been widely proved that the NLO responses of polar crystals are directly attributed to the polarization of NLO-active motifs.[11a,15] Herein, the polarization of the compound was evaluated by measuring the SHG response. The SHG signal of the polycrystalline sample was collected by using the Kurtz–Perry method under 2090 nm pulse laser with $AgGaS_2$ crystals as reference.[16] As depicted in Figure 3a and S5, the SHG intensity of the as-synthesized $Sr_6Cd_2Sb_6O_7Se_{10}$ crystals with the size range of 20–41 μm is 12.6 times that of $AgGaS_2$, while in 105–150 and 150–200 μm the SHG responses are also larger than those of $AgGaS_2$ (2.1 and 1.8 times, respectively), indicating strong polarization of the material. The SHG responses of the single crystal were also measured. The wavelength dependence of

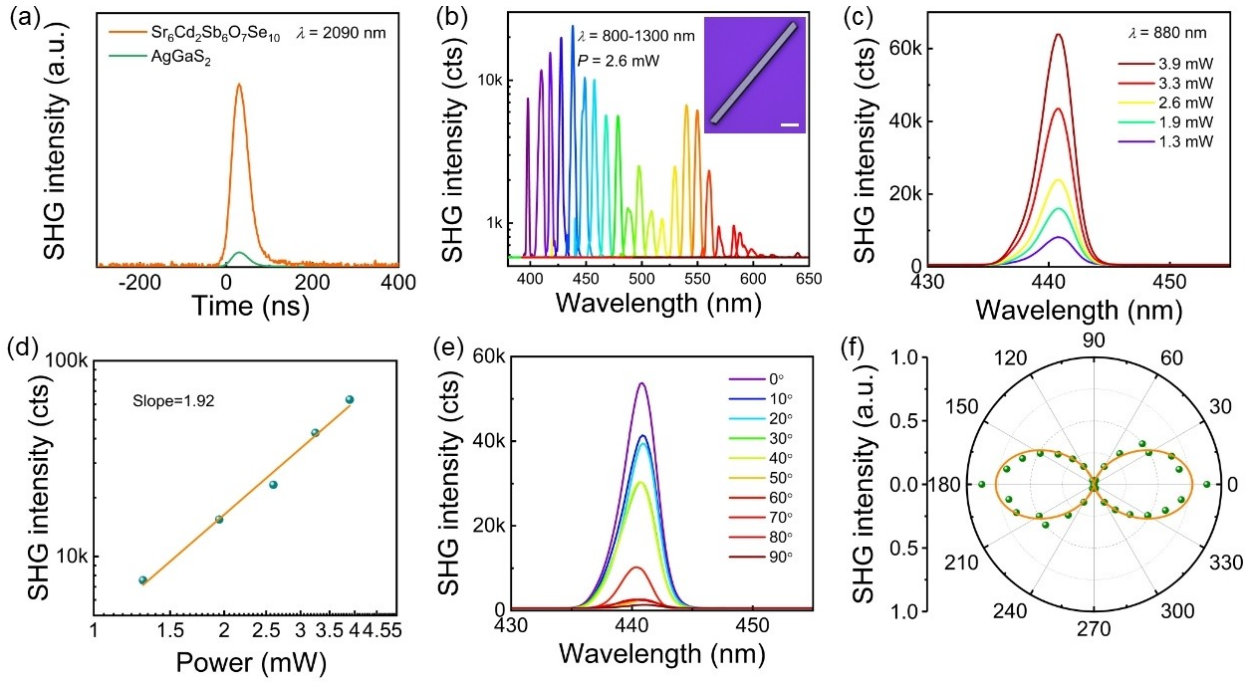

Figure 3. a) SHG signal of powder sample and $AgGaS_2$ (reference) under 2090 nm laser irradiation. b) Evolution of single-crystal SHG intensity with the excitation wavelength ranging from 800 nm to 1300 nm. Inset: the optical micrograph of the single crystal with a scale bar of 20 μm. c) Power-dependent SHG intensity excited by 880 nm laser. d) Power dependence of the maximum SHG intensity in logarithmic coordinates. Angle dependence of the polarized SHG intensity under parallel configurations in e) 0–90° and f) 0–360°.

SHG intensity was investigated in the excitation range of 800–1300 nm with a step of 20 nm. As depicted in Figure 3b, large SHG signals were detected in a broadband wavelength range. The intensity reached the maximum under the radiation of 880 nm laser. While the transmittance of the single crystal between 400 and 700 nm is relatively low (Figure S6), the SHG signals in this region were still strong enough to be detected, indicating the intense polarization of this material. The power-dependent SHG response of the single crystal was also obtained under 880 nm laser in the power range of 1.3–3.9 mW, as illustrated in Figure 3c. The SHG intensity under different radiation power can be well linearly fitted in logarithmic coordinates with a fitted slope of 1.92 (Figure 3d), which is in good agreement with the theoretical value 2 originating from the two-photon nature of second-order NLO process.[17] The angle-resolved polarized SHG (ARPSHG) measurement was conducted to reveal the polarization-dependent SHG properties. An analyzer with the orientation parallel to the incident laser polarization was placed in front of the detector. The rotation angle θ was defined as the angle between the incident laser polarization direction and the long side of the rod-like crystal. The results show that the SHG intensity decreases along with the rotation of the crystal from $\theta=0$ to 90° (Figure 3e). The SHG polar map under the parallel polarization configuration shows a two-lobed pattern (Figure 3f), which is consistent with the symmetry of crystal class *m* revealed by the X-ray diffraction measurement.[18] The large SHG response implies strong polarization of the material which is beneficial to the charge separation in the photoelectric process. Meanwhile, the polarization-dependent SHG behavior indicates the potential application of this material for polarization-dependent NLO devices.

In order to evaluate the prospect of this material for photoelectric conversion application, we investigated its semiconductive properties. Other properties of the material were discussed in the Supporting Information. The room-temperature optical absorption spectrum (Figure S7) showed a sharp absorption edge near 750 nm, and the band gap was determined to be 1.55 eV by an extrapolation method using the Kubelka–Munk equation (Figure 4a).[19] This band gap is smaller than the sulfide $Sr_6Cd_2Sb_6O_7S_{10}$ (1.89 eV),[8f] and thus more suitable for the absorption and conversion of visible light. The band alignment of $Sr_6Cd_2Sb_6O_7Se_{10}$ was assessed by ultraviolet photoelectron spectroscopy (UPS) measurements. The binding energy was calibrated by setting the Fermi level (E_F) of a clean Au reference at 0 V. As shown in Figure 4b, the secondary electron cutoff binding energy E_{cutoff} is 17.02 eV, which was determined by linearly extrapolating the leading edge. The work function $\Phi=4.20$ eV can be estimated under the formula $\Phi=h\nu-E_{cutoff}$ (where h is the Planck constant and ν is the frequency of excitation light, here $h\nu=21.22$ eV). The E_F of the sample should be -4.20 eV versus the vacuum level. Moreover, the valence band energy $E_{VB}=0.67$ eV can be determined by the intersection of the linear extrapolation of the valence band edge and the baseline. After determining the optical band gap (1.55 eV) and the valence-band position (0.67 eV), the conduction band position E_{CB} can be obtained following the relationship $E_g=E_{VB}-E_{CB}$. All the measured components are illustrated in the band diagram in Figure 4c. The measured valence band edge -4.87 eV vs. vacuum level is similar to those of materials containing lone-

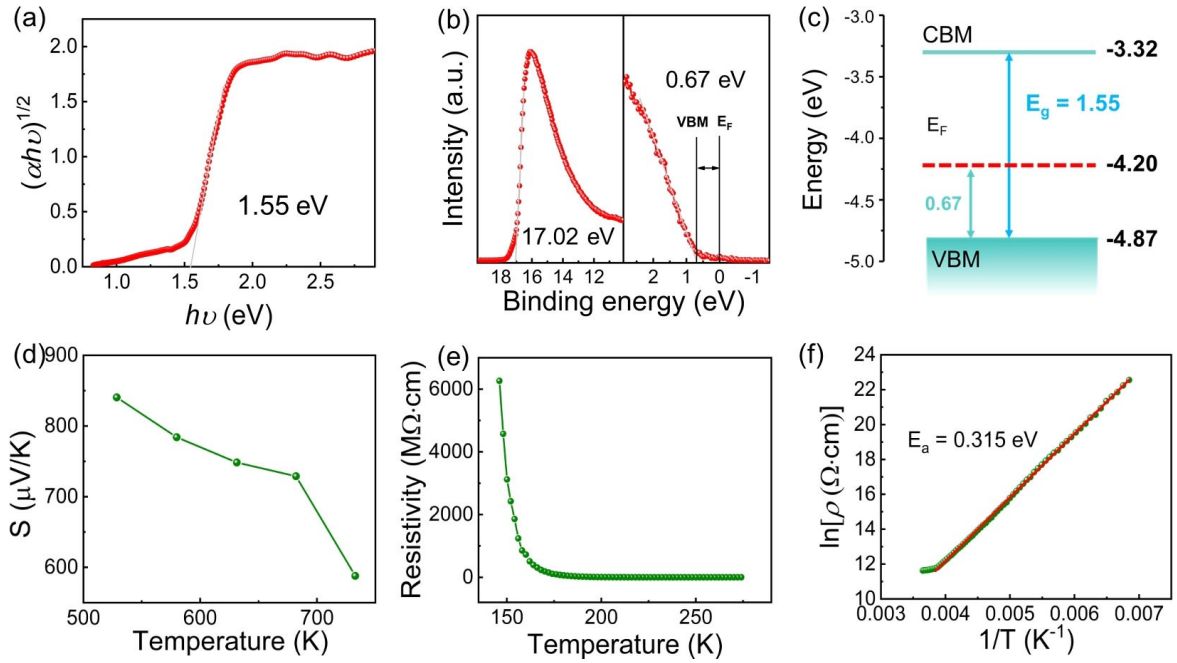

Figure 4. a) Plot of $(\alpha h\nu)^{1/2}$ vs. energy converting using the Kubelka–Munk equation. b) UPS spectrum for work function (left) and valence band edge (right). c) The macroscopic band diagram of $Sr_6Cd_2Sb_6O_7Se_{10}$. Temperature dependence of d) the Seebeck coefficient and e) the single-crystal electrical resistivity. f) Arrhenius fitting of the resistivity curve ($E_a=0.315$ eV).

pair electrons.[20] Considering the position of the Fermi level, the as-synthesized $Sr_6Cd_2Sb_6O_7Se_{10}$ should be a *p*-type semiconductor.

The p-type conductive nature of the material was further confirmed by the positive Seebeck coefficient measured on the spark plasma sintered (SPSed) pellet (Figure 4d). The phase purity of the pellet was checked by PXRD measurement (Figure S8). The Seebeck coefficient showed negative temperature dependence, which decreased from 840 $\mu V K^{-1}$ at 529 K to 588 $\mu V K^{-1}$ at 733 K. The high-temperature dependence of electrical resistivity showed typical thermally activated conduction behavior (Figure S9). A single crystal (Figure S10) was picked out to measure the low-temperature electrical resistivity, and the result is shown in Figure 4e. We noted that in the temperature range of 146–260 K, the resistivity follows the Arrhenius dependence $\rho(T)=\rho_0 \exp(E_a/k_B T)$, where E_a is the activation energy (Figure 4f). The activation energy was estimated to be 0.315 eV. Compared with the band gap 1.55 eV, this activation energy is much smaller, indicating that the transport process is associated with the ionization of defect states lying in the band gap.

In aim to identify the possible defect states and determine the optical quality of the as-synthesized material, photoluminescence (PL) measurements were conducted on the $Sr_6Cd_2Sb_6O_7Se_{10}$ single crystal at room and low temperature. The room-temperature PL spectrum under 532 nm excitation showed three broad emission bands which can be modeled by four Gaussian peaks centered at 1.34 eV (peak 1), 1.48 eV (peak 2), 1.61 eV (peak 3) and 1.65 eV (peak 4) (Figure 5a). Peak 1 and 2 both lie below the band edge (1.55 eV), while peak 3 and 4 are slightly above the band gap. The PL spectrum with 633 nm excitation showed similar emission bands (Figure S11). The as-fitted peaks 1–3 revealed no obvious shifting compared with those under 532 nm, while peak 4 possessed slight blue-shift from 1.65 eV to 1.72 eV. The below-band gap emission indicates the existence of shallow defect levels in the band gap. The above-band gap emission peak 3 and 4 correspond to the same broad band and could be presumably ascribed to the excitonic emission related to the defect states below the VBM or above the CBM. These above-band gap PL emissions have also been observed on perovskite halides $MAPbI_3$, $CsPbBr_3$, $TlPbI_3$ and dilute $GaAs_{1-x}N_x$ alloys and $GaAs_{1-x}P_x$.[21] As the emission bands of $Sr_6Cd_2Sb_6O_7Se_{10}$ are close to the band gap, the $[Sb_2OSe_4]^{4-}$ chain (sublattice I) which mainly contributes to the band edges should be the PL-active emitter.

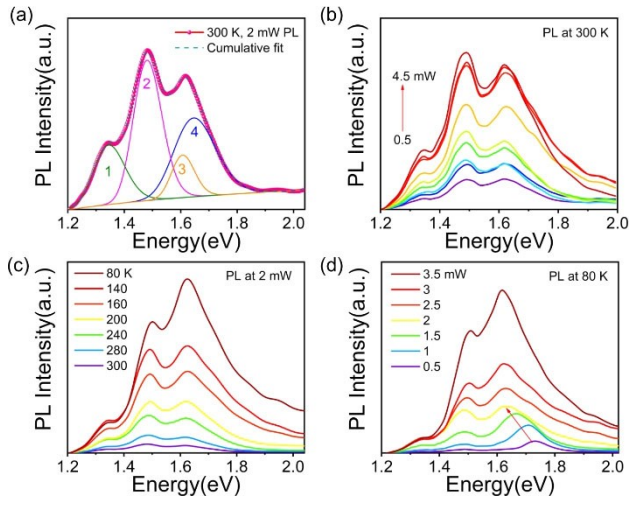

Figure 5. a) Room-temperature PL spectrum of the single crystal. The emission band was fitted by four Gaussian emission peaks (peak 1, 2, 3 and 4). b) Dependence of the PL spectra on laser power at 300 K. c) Temperature dependence of the PL spectra at 2 mW. d) Power dependence of the PL spectra at 80 K.

The origin of the PL emission was investigated by the PL dependence on excitation intensity and temperature. The power-dependent PL intensity at room temperature was collected by increasing the laser power from 0.5 mW to 4.5 mW, resulting in corresponding intensity enhancements (Figure 5b). The PL intensity I follows a power-law dependence on excitation intensity L as $I \propto L^k$, governed by the exponent k.[22] For the excitonic emission the exponent is in the range of $1<k<2$, while free-to-bound and donor-acceptor pair (DAP) recombination give the k value below 1. The plots of log$I$ versus log$L$ of peak 1 and 2 are shown in Figure S12 which give the power-law coefficients both below 1, indicating they are generated by either free-to-bound or DAP recombination. As the log$I$ versus log$L$ plots of peak 3 and 4 do not show reliable linear dependence, low-temperature PL tests were conducted to reveal the origin of these radiative transitions. The temperature dependence behavior in Figure 5c showed that the intensity of all the peaks are enhanced by decreasing temperature, while the broad band composed of peak 3 and 4 displays more significant growth than the other two and becomes the strongest emission at 80 K. The power-dependent PL spectra at 80 K in Figure 5d revealed an obvious redshift of the highest-energy broad band excited by laser power from 0.5 mW to 2.0 mW, which is significantly different from the other two bands with no clear peak-shifting trend. These results combined with the above-band gap character indicate that the highest emission band possesses different origination from the other two bands, which could be generated by the excitonic recombination. Furthermore, the room-temperature excitonic emission suggests a high exciton binding energy which should involve bound exciton recombination. Nevertheless, the strong room-temperature PL emission from an indirect-band-gap semiconductor is evidence of its good optical quality. More importantly, no prominent deep-level emission was observed in the range of 0.80–1.20 eV as revealed by Figure S11 and S13. These results indicate that the concentrations of the defects for the deep level emissions in that range are negligible, which is beneficial to the efficient charge carrier transport in this material.

The efficient charge carrier separation promoted by the polar sublattices in $Sr_6Cd_2Sb_6O_7Se_{10}$ was further clarified by the enhanced carrier lifetime and photoelectric response compared with those of the nonpolar oxyselenide $Sr_2Sb_2O_2Se_3$ ($P2_1/c$).[23] $Sr_2Sb_2O_2Se_3$ is a close-related compound of $Sr_6Cd_2Sb_6O_7Se_{10}$. As shown in Figure 6a, it is composed of the sublattice of double tetragonal-pyramid

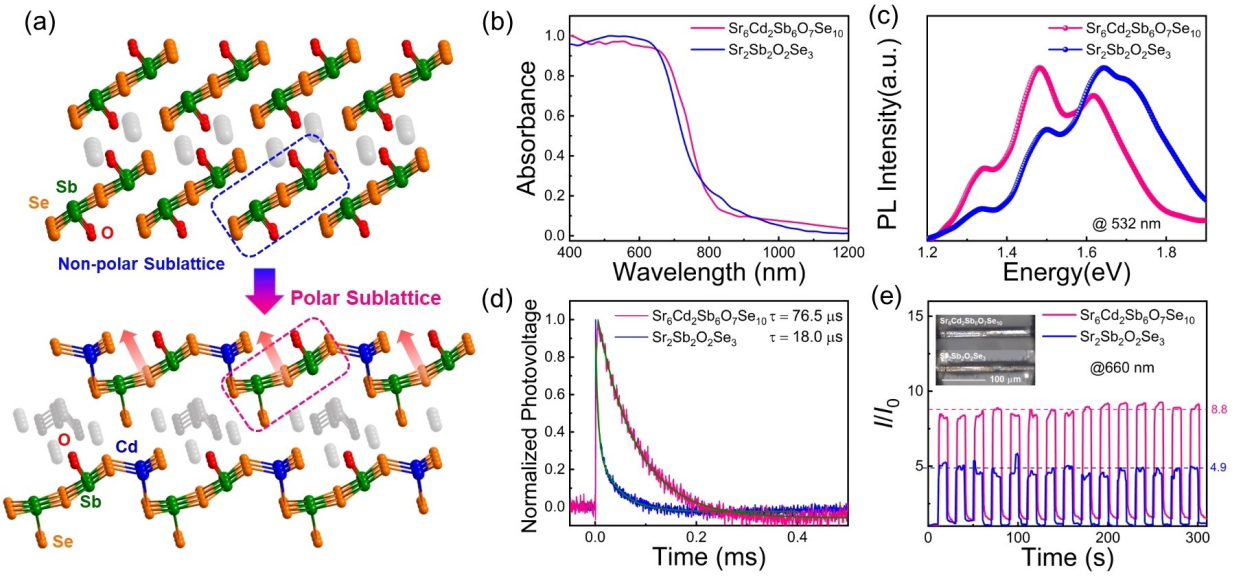

Figure 6. a) The structure comparison between $Sr_2Sb_2O_2Se_3$ and $Sr_6Cd_2Sb_6O_7Se_{10}$. The blue and red frames represent the nonpolar $[Sb_2O_2Se_3]^{4-}$ chain and polar $[Sb_2OSe_4]^{4-}$ chain, respectively. b) UV/Vis-NIR absorption and c) PL emission spectra of $Sr_6Cd_2Sb_6O_7Se_{10}$ and $Sr_2Sb_2O_2Se_3$. d) TPV decay curves of $Sr_6Cd_2Sb_6O_7Se_{10}$ and $Sr_2Sb_2O_2Se_3$ under open circuit condition. e) The current density ratio (I/I_0) of single-crystal devices of $Sr_2Sb_2O_2Se_3$ and $Sr_6Cd_2Sb_6O_7Se_{10}$ under 660 nm illumination with the bias voltage of 5 V; inset: the photographs of the single-crystal devices.

$[Sb_2O_2Se_3]^{4-}$ chain which is similar to $[Sb_2OSe_4]^{4-}$ chain (sublattice I) in $Sr_6Cd_2Sb_6O_7Se_{10}$. The major difference between them is that the dipole moment of $[Sb_2O_2Se_3]^{4-}$ chain is canceled by the two adjacent $[SbOSe_4]^{7-}$ units with opposite orientation, while substituting one O with Se can break the centrosymmetry and generate spontaneous polarization in the $[Sb_2OSe_4]^{4-}$ chain. As these sublattices are the main contributors to the band edges, they play decisive roles in the optical and electronic properties of the two compounds. Thus, this structure difference between the two materials provides an ideal platform to evaluate the influence of polarization on their carrier recombination dynamics.

$Sr_2Sb_2O_2Se_3$ was obtained via solid-state reaction at 700 °C as reported. The phase purity of the product was confirmed by PXRD (Figure S14a). Rod-like single crystals of $Sr_2Sb_2O_2Se_3$ (Figure S14b: SEM image and EDX mapping analysis) were grown for single-crystal PL spectroscopy measurement. $Sr_2Sb_2O_2Se_3$ possesses a similar band gap with $Sr_6Cd_2Sb_6O_7Se_{10}$ revealed by UV/Vis-NIR absorption spectra (Figure 6b). PL emission bands of the $Sr_2Sb_2O_2Se_3$ single crystal can be modeled by four Gaussian peaks centered at 1.33 eV, 1.49 eV, 1.61 eV and 1.70 eV (Figure S15) which are also close to those of $Sr_6Cd_2Sb_6O_7Se_{10}$ (Figure 6c), indicating the similar origin of these PL emissions. These results demonstrated their similar band compositions and defect states near the band edges.

While the two materials possess similar optical properties, the structure evolution from $Sr_2Sb_2O_2Se_3$ to $Sr_6Cd_2Sb_6O_7Se_{10}$ significantly influences the carrier recombination dynamics and photoelectric conversion process. The carrier recombination lifetimes of the two materials were compared by measuring their transient photovoltage decay (TPV) under open circuit condition. The photovoltage decay curves of the polycrystalline samples are plotted in Figure 6d, showing a much slower recombination rate of $Sr_6Cd_2Sb_6O_7Se_{10}$ than that of $Sr_2Sb_2O_2Se_3$. The carrier recombination lifetime of $Sr_6Cd_2Sb_6O_7Se_{10}$ was estimated to be 76.5 μs extracted from a mono-exponential fit, as listed in Table S3. The decay curve of $Sr_2Sb_2O_2Se_3$ was fitted by bi-exponential function which gives two lifetimes of $\tau_1 = 4.9$ μs (64.0 %) and $\tau_2 = 41.3$ μs (36.0 %). The average recombination lifetime τ_{ave} of $Sr_2Sb_2O_2Se_3$ was estimated to be 18.0 μs. The prolonged τ represents the suppressed nonradiative recombination. The PL decay traces obtained from the time-resolved PL spectroscopy (TRPL) also reveal a longer PL lifetime of $Sr_6Cd_2Sb_6O_7Se_{10}$ than that of $Sr_2Sb_2O_2Se_3$ (Figure S16), indicating the high carrier separation efficiency promoted by the polarization field in $Sr_6Cd_2Sb_6O_7Se_{10}$. Moreover, single crystals of $Sr_6Cd_2Sb_6O_7Se_{10}$ and $Sr_2Sb_2O_2Se_3$ with similar sizes (Figure S17) were picked out to measure their photoelectric responses. The I/I_0 ratio curves (I *is* the current density of the device, I_0 is the current density measured in dark) in Figure 6e and S18 revealed that the $Sr_6Cd_2Sb_6O_7Se_{10}$-based device shows almost twice larger I/I_0 maximum than that of the $Sr_2Sb_2O_2Se_3$-based device under 660 and 532 nm illumination. The photoelectric response measurements performed on ceramic plates of the two materials (Figure S19) also give consistent results. These results corroborate the efficient carrier separation in the polar material $Sr_6Cd_2Sb_6O_7Se_{10}$ for promising photoelectric application.

The detailed photoelectric conversion performance of $Sr_6Cd_2Sb_6O_7Se_{10}$ was further explored based on a single-crystal device as shown in the inset of Figure 7a. The Ohmic contact of the circuit was confirmed by the linear dependence of the I–V curves in Figure 7a, which is favorable for electron transmission. The device displayed large and differ-

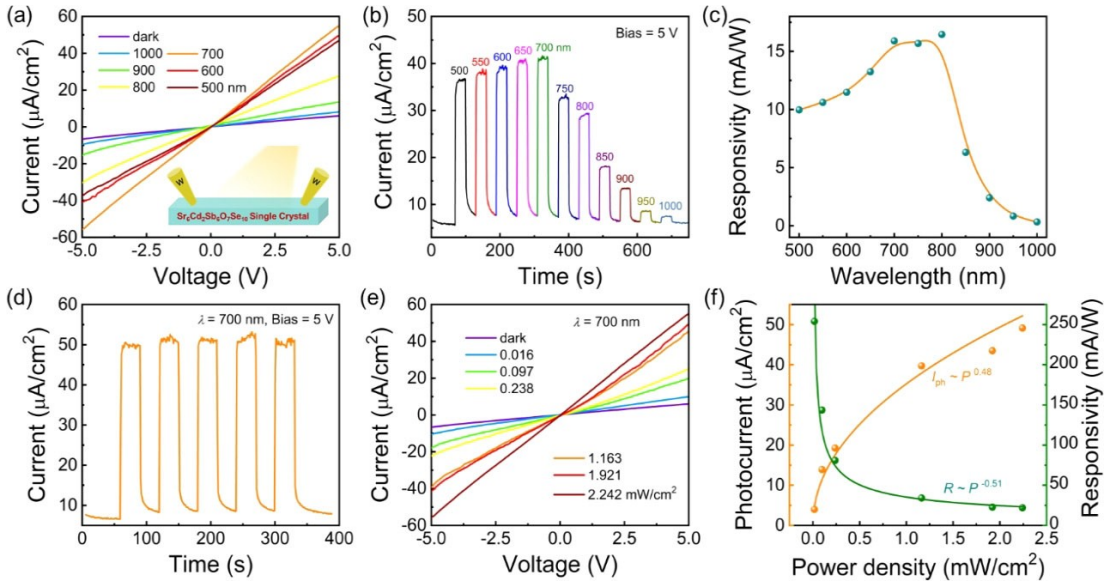

Figure 7. Photoelectric properties of the $Sr_6Cd_2Sb_6O_7Se_{10}$ single crystal. a) *I–V* curves of the single crystal measured in dark and under illumination with various incident wavelengths of 500 to 1000 nm. The inset is the schematic diagram of the single-crystal device. b) Time-resolved photoresponse under excitation of various wavelengths with different power. c) Wavelength-dependent responsivity of the single crystal at $V_{bias} = 5$ V. d) Time-resolved photoresponse under 700 nm light irradiation at $V_{bias} = 5$ V. e) *I–V* curves of the single crystal measured in dark and under 700 nm illumination with different light intensity. f) Photocurrent and responsivity as a function of light intensity.

ent current enhancement under the illumination of varying incident wavelengths in 500–1000 nm, indicating remarkable photoresponse in a broadband range. The time-resolved photocurrent depicted in Figure 7b further confirmed the stable and broadband photoresponse. The responsivity ($R = I_{ph}/PS$, where I_{ph} represents photocurrent $I_{ph} = I_{light} - I_{dark}$, I_{light} and I_{dark} are the current densities under illumination and in dark, respectively, P represents power density of the light and S represents the illuminated area.) of the device at different incident wavelengths is shown in Figure 7c, which reached the maximum of 15 mA W^{-1} near 800 nm and decreased in longer wavelength. The evolution of wavelength-dependent responsivity corresponds to the optical absorption spectrum of the material. The detectable photoresponse under 850–1000 nm light could originate from the defect-related excitation which has been revealed by the PL spectrum. The electrons in the defect states can be excited to the conduction band by below-band-gap light, producing a measurable photoresponse beyond the absorption edge, further extending the response range. The sub-band-gap photoresponses were also observed in other photoelectric materials containing shallow defect states like $CH_3NH_3PbX_3$ (X = Br, I) and Bi_2S_3.[24] The stability of the photoresponse behavior under different incident wavelengths of 500–1000 nm was investigated by periodically switching the light on/off every 30 s at a bias of 5 V, as shown in Figure 7d and S20. The results showed that the on/off switching behavior maintains well in the holding time of 400 s, indicating stable repeatability of the device in broad spectral range.

The correlation between the light intensity and photocurrent was investigated using 700 nm incident light. Figure 7e presented the *I–V* characteristics of the single-crystal device measured in dark and under irradiation of various power densities from 0.016 to 2.242 mW cm^{-2}. The current increased gradually along with the increasing light intensity, which should own to enhancing photo-induced charge carriers. The largest on/off current ratio (I_{ph}/I_{dark}) is approximately 8.2 at light intensity of 2.242 mW cm^{-2}, implying remarkable photoresponse of the device. The light intensity dependence of the photocurrent and responsivity were plotted in Figure 7f. The two curves can be well fitted by the power law as $I_{ph} \approx P^{0.48}$ and $R \approx P^{-0.51}$, respectively. The sublinear dependence can be regarded as a result of the complex processes of the generation, trapping, recombination and transportation of the photo-induced electron-hole pairs, which were also observed in other photoelectric materials.[25] These results demonstrate the significant potential of this material for photoelectric applications. The photoresponse performance can be further improved by optimizing the device fabrication such as reducing the thickness of the crystal for better on/off current ratio and responsivity.

Conclusion

In summary, a novel polar oxyselenide $Sr_6Cd_2Sb_6O_7Se_{10}$ with lateral sublattices was rationally designed and synthesized. The sublattices are constructed by polarizable $[Sb_2OSe_4]^{4-}$ chains and highly-orientated $[CdSe_3]^{4-}$ chains. This compound possesses a suitable band gap for photoelectric conversion, good crystal quality with strong PL emission and intense polarization with large SHG intensity. The single-crystal device showed excellent photoelectric properties with broadband photoresponse and stable reproducibility. This work not only provides a new promising photoelectric

conversion material, but may ignite the exploration of new polar heteroanionic materials for technological implementation of solar energy conversion.

Acknowledgements

This work was financially supported by the National Natural Science Foundation of China (Grant 22005006, 22001263, 21871008, 21825103), the China Postdoctoral Science Foundation (Grant 2019M660298, 2020T130009). We would thank Dr. Y. W. Guo for his support on the powder SHG effect measurement. We would thank the analytical instrumentation center of college of chemistry and molecular engineering (CCME) for supporting the PL, XPS and TGA-DSC measurements.

Conflict of Interest

The authors declare no conflict of interest.

Data Availability Statement

The data that support the findings of this study are available from the corresponding author upon reasonable request.

Keywords: Heteroanionic Compounds · Photoelectric Conversion · Polarization · Second-Harmonic Generation

[1] a) C. Gao, T. Wei, Y. Zhang, X. Song, Y. Huan, H. Liu, M. Zhao, J. Yu, X. Chen, *Adv. Mater.* **2019**, *31*, 1806596; b) X. Hong, J. Kim, S.-F. Shi, Y. Zhang, C. Jin, Y. Sun, S. Tongay, J. Wu, Y. Zhang, F. Wang, *Nat. Nanotechnol.* **2014**, *9*, 682–686; c) J. Low, J. Yu, M. Jaroniec, S. Wageh, A. A. Al-Ghamdi, *Adv. Mater.* **2017**, *29*, 1601694.

[2] a) X. Fan, L. Zang, M. Zhang, H. Qiu, Z. Wang, J. Yin, H. Jia, S. Pan, C. Wang, *Chem. Mater.* **2014**, *26*, 3169–3174; b) G. Gou, M. Zhao, J. Shi, J. K. Harada, J. M. Rondinelli, *Chem. Mater.* **2020**, *32*, 2815–2823; c) X. He, C. Chen, C. Li, H. Zeng, Z. Yi, *Adv. Funct. Mater.* **2019**, *29*, 1900918; d) C. Hu, H. Huang, F. Chen, Y. Zhang, H. Yu, T. Ma, *Adv. Funct. Mater.* **2020**, *30*, 1908168; e) H. Huang, S. Tu, C. Zeng, T. Zhang, A. H. Reshak, Y. Zhang, *Angew. Chem. Int. Ed.* **2017**, *56*, 11860–11864; *Angew. Chem.* **2017**, *129*, 12022–12026; f) Z. Lou, B. Huang, Z. Wang, X. Ma, R. Zhang, X. Zhang, X. Qin, Y. Dai, M.-H. Whangbo, *Chem. Mater.* **2014**, *26*, 3873–3875; g) L. Lv, F. Zhuge, F. Xie, X. Xiong, Q. Zhang, N. Zhang, Y. Huang, T. Zhai, *Nat. Commun.* **2019**, *10*, 3331; h) G. Zhang, H. Wu, G. Li, Q. Huang, C. Yang, F. Huang, F. Liao, J. Lin, *Sci. Rep.* **2013**, *3*, 1265.

[3] W. Yang, Y. Yu, M. B. Starr, X. Yin, Z. Li, A. Kvit, S. Wang, P. Zhao, X. Wang, *Nano Lett.* **2015**, *15*, 7574–7580.

[4] H. Ying, X. Li, H. Wang, Y. Wang, X. Hu, J. Zhang, X. Zhang, Y. Shi, M. Xu, Q. Zhang, *Adv. Opt. Mater.* **2020**, *8*, 2000430.

[5] a) Z. A. Gál, O. J. Rutt, C. F. Smura, T. P. Overton, N. Barrier, S. J. Clarke, J. Hadermann, *J. Am. Chem. Soc.* **2006**, *128*, 8530–8540; b) T. Sambrook, C. F. Smura, S. J. Clarke, K. M. Ok, P. S. Halasyamani, *Inorg. Chem.* **2007**, *46*, 2571–2574; c) C. F. Smura, D. R. Parker, M. Zbiri, M. R. Johnson, Z. A. Gál, S. J. Clarke, *J. Am. Chem. Soc.* **2011**, *133*, 2691–2705.

[6] a) K. Bu, J. Huang, M. Luo, M. Guan, C. Zheng, J. Pan, X. Zhang, S. Wang, W. Zhao, X. Shi, L. Xu, F. Huang, *Chem. Mater.* **2018**, *30*, 5539–5543; b) H. Hiramatsu, H. Yanagi, T. Kamiya, K. Ueda, M. Hirano, H. Hosono, *Chem. Mater.* **2008**, *20*, 326–334; c) A. Ishikawa, T. Takata, J. N. Kondo, M. Hara, H. Kobayashi, K. Domen, *J. Am. Chem. Soc.* **2002**, *124*, 13547–13553; d) X. Lu, N. Wang, H. Wu, Y. Wu, D. Zhao, X. Zeng, X. Luo, T. Wu, W. Bao, G. Zhang, *Nat. Mater.* **2015**, *14*, 325–329; e) A. Miura, T. Oshima, K. Maeda, Y. Mizuguchi, C. Moriyoshi, Y. Kuroiwa, Y. Meng, X.-D. Wen, M. Nagao, M. Higuchi, *J. Mater. Chem. A* **2017**, *5*, 14270–14277.

[7] H. Kageyama, K. Hayashi, K. Maeda, J. P. Attfield, Z. Hiroi, J. M. Rondinelli, K. R. Poeppelmeier, *Nat. Commun.* **2018**, *9*, 772.

[8] a) W. Xing, P. Fang, N. Wang, Z. Li, Z. Lin, J. Yao, W. Yin, B. Kang, *Inorg. Chem.* **2020**, *59*, 16716–16724; b) R. Wang, Y. Guo, X. Zhang, Y. Xiao, J. Yao, F. Huang, *Inorg. Chem.* **2020**, *59*, 9944–9950; c) X. Zhang, L. Kang, P. Gong, Z. Lin, Y. Wu, *Angew. Chem. Int. Ed.* **2021**, *60*, 6386–6390; *Angew. Chem.* **2021**, *133*, 6456–6460; d) H. Yan, Y. Matsushita, K. Yamaura, Y. Tsujimoto, *Angew. Chem. Int. Ed.* **2021**, *60*, 26561–26565; *Angew. Chem.* **2021**, *133*, 26765–26769; e) J. Wang, Y. Cheng, H. Wu, Z. Hu, J. Wang, Y. Wu, H. Yu, *Angew. Chem. Int. Ed.* **2022**, *61*, e202201616; *Angew. Chem.* **2022**, *134*, e202201616; f) R. Wang, F. Liang, F. Wang, Y. Guo, X. Zhang, Y. Xiao, K. Bu, Z. Lin, J. Yao, T. Zhai, F. Huang, *Angew. Chem. Int. Ed.* **2019**, *58*, 8078–8081; *Angew. Chem.* **2019**, *131*, 8162–8165.

[9] a) A. Mavlonov, T. Razykov, F. Raziq, J. Gan, J. Chantana, Y. Kawano, T. Nishimura, H. Wei, A. Zakutayev, T. Minemoto, *Sol. Energy* **2020**, *201*, 227–246; b) U. Woggon, *Optical properties of semiconductor quantum dots, Vol. 136*, Springer, Heidelberg, **1997**.

[10] Deposition Number 2091885 contains the supplementary crystallographic data for this paper. These data are provided free of charge by the joint Cambridge Crystallographic Data Centre and Fachinformationszentrum Karlsruhe Access Structures service.

[11] a) J. Goodey, J. Broussard, P. S. Halasyamani, *Chem. Mater.* **2002**, *14*, 3174–3180; b) P. A. Maggard, T. S. Nault, C. L. Stern, K. R. Poeppelmeier, *J. Solid State Chem.* **2003**, *175*, 27–33.

[12] a) M. Liu, D. Jing, Z. Zhou, L. Guo, *Nat. Commun.* **2013**, *4*, 2278; b) M. Liu, L. Wang, G. M. Lu, X. Yao, L. Guo, *Energy Environ. Sci.* **2011**, *4*, 1372–1378; c) A. Onen, D. Kecik, E. Durgun, S. Ciraci, *J. Phys. Chem. C* **2017**, *121*, 27098–27110; d) A. Onen, D. Kecik, E. Durgun, S. Ciraci, *Phys. Rev. B* **2017**, *95*, 155435.

[13] a) A. Iwaszuk, M. Nolan, *J. Mater. Chem. A* **2013**, *1*, 6670–6677; b) T. Li, S. Luo, X. Wang, L. Zhang, *Adv. Mater.* **2021**, *33*, 2008574.

[14] a) M. Yan, H.-G. Xue, S.-P. Guo, *Cryst. Growth Des.* **2021**, *21*, 698–720; b) B. Du, R. Zhang, K. Chen, A. Mahajan, M. J. Reece, *J. Mater. Chem. A* **2017**, *5*, 3249–3259; c) G. Tan, L.-D. Zhao, M. G. Kanatzidis, *Chem. Rev.* **2016**, *116*, 12123–12149.

[15] H.-S. Ra, K. M. Ok, P. S. Halasyamani, *J. Am. Chem. Soc.* **2003**, *125*, 7764–7765.

[16] S. Kurtz, T. Perry, *J. Appl. Phys.* **1968**, *39*, 3798–3813.

[17] a) Y. Fang, X. Hu, W. Zhao, J. Pan, D. Wang, K. Bu, Y. Mao, S. Chu, P. Liu, T. Zhai, *J. Am. Chem. Soc.* **2019**, *141*, 790–793; b) X. Feng, Z. Sun, K. Pei, W. Han, F. Wang, P. Luo, J. Su, N. Zuo, G. Liu, H. Li, *Adv. Mater.* **2020**, *32*, 2003146; c) D. Fu, J. Xin, Y. He, S. Wu, X. Zhang, X. M. Zhang, J. Luo, *Angew. Chem. Int. Ed.* **2021**, *60*, 20021–20026; *Angew. Chem.* **2021**, *133*, 20174–20179; d) F. Ge, B.-H. Li, P. Cheng, G. Li, Z. Ren, J. Xu, X.-H. Bu, *Angew. Chem. Int. Ed.* **2022**, *61*, e202115024;

Angew. Chem. **2022**, *134*, e202115024; e) Y. Zheng, J. Xu, X. H. Bu, *Adv. Opt. Mater.* **2022**, *10*, 2101545.

[18] R. Beams, L. G. Cançado, S. Krylyuk, I. Kalish, B. Kalanyan, A. K. Singh, K. Choudhary, A. Bruma, P. M. Vora, F. Tavazza, *ACS Nano* **2016**, *10*, 9626–9636.

[19] G. Kortüm, W. Braun, G. Herzog, *Angew. Chem. Int. Ed. Engl.* **1963**, *2*, 333–341; *Angew. Chem.* **1963**, *75*, 653–661.

[20] C. H. Don, H. Shiel, T. D. Hobson, C. N. Savory, J. E. Swallow, M. J. Smiles, L. A. Jones, T. J. Featherstone, P. K. Thakur, T.-L. Lee, *J. Mater. Chem. C* **2020**, *8*, 12615–12622.

[21] a) Q. Dong, Y. Fang, Y. Shao, P. Mulligan, J. Qiu, L. Cao, J. Huang, *Science* **2015**, *347*, 967–970; b) W. Lin, J. He, K. M. McCall, C. C. Stoumpos, Z. Liu, I. Hadar, S. Das, H. H. Wang, B. X. Wang, D. Y. Chung, *Adv. Funct. Mater.* **2021**, *31*, 2006635; c) D. Scifres, N. Holonyak Jr, C. Duke, G. Kleiman, A. Kunz, M. Craford, W. Groves, A. Herzog, *Phys. Rev. Lett.* **1971**, *27*, 191; d) M. Sebastian, J. Peters, C. Stoumpos, J. Im, S. Kostina, Z. Liu, M. G. Kanatzidis, A. J. Freeman, B. Wessels, *Phys. Rev. B* **2015**, *92*, 235210; e) P. Tan, X. Luo, Z. Xu, Y. Zhang, A. Mascarenhas, H. Xin, C. Tu, W. Ge, *Phys. Rev. B* **2006**, *73*, 205205.

[22] T. Schmidt, K. Lischka, W. Zulehner, *Phys. Rev. B* **1992**, *45*, 8989.

[23] J. R. Panella, J. Chamorro, T. M. McQueen, *Chem. Mater.* **2016**, *28*, 890–895.

[24] a) Q. Lin, A. Armin, P. L. Burn, P. Meredith, *Laser Photonics Rev.* **2016**, *10*, 1047–1053; b) N. Huo, A. Figueroba, Y. Yang, S. Christodoulou, A. Stavrinadis, C. Magén, G. Konstantatos, *Adv. Opt. Mater.* **2019**, *7*, 1900258.

[25] a) S. R. Tamalampudi, Y.-Y. Lu, R. K. U, R. Sankar, C.-D. Liao, C.-H. Cheng, F. C. Chou, Y.-T. Chen, *Nano Lett.* **2014**, *14*, 2800–2806; b) F. Wang, T. Gao, Q. Zhang, Z. Y. Hu, B. Jin, L. Li, X. Zhou, H. Li, G. Van Tendeloo, T. Zhai, *Adv. Mater.* **2019**, *31*, 1806306; c) H. Song, T. Li, J. Zhang, Y. Zhou, J. Luo, C. Chen, B. Yang, C. Ge, Y. Wu, J. Tang, *Adv. Mater.* **2017**, *29*, 1700441.

Manuscript received: May 9, 2022
Accepted manuscript online: June 17, 2022
Version of record online: July 8, 2022